Dislocation-Driven Deformations in Graphene

Jamie H. Warner *et al.*
Science **337**, 209 (2012);
DOI: 10.1126/science.1217529

24. P. N. Murgatroyd, *J. Phys. D* **3**, 151 (1970).
25. D. Sun *et al.*, *Phys. Rev. Lett.* **104**, 236602 (2010).

Dislocation-Driven Deformations in Graphene

Jamie H. Warner,[1]* Elena Roxana Margine,[1] Masaki Mukai,[2] Alexander W. Robertson,[1] Feliciano Giustino,[1] Angus I. Kirkland[1]

The movement of dislocations in a crystal is the key mechanism for plastic deformation in all materials. Studies of dislocations have focused on three-dimensional materials, and there is little experimental evidence regarding the dynamics of dislocations and their impact at the atomic level on the lattice structure of graphene. We studied the dynamics of dislocation pairs in graphene, recorded with single-atom sensitivity. We examined stepwise dislocation movement along the zig-zag lattice direction mediated either by a single bond rotation or through the loss of two carbon atoms. The strain fields were determined, showing how dislocations deform graphene by elongation and compression of C-C bonds, shear, and lattice rotations.

The two-dimensional (2D) structure of graphene provides unusual mechanical (*1*) and electronic properties (*2*), which can be influenced by defects and dislocations (*3*, *4*). Defects and strain can lead to spin and magnetism in graphene that may be important for extending graphene's electronic applications into spin-based technology (*5*, *6*). Understanding how dislocations deform graphene helps build an accurate description of both elasticity and plasticity in graphene (*7–9*). Studying dislocation movement (creep and climb), the interaction between dislocation pairs, and how the strain fields respond is key for developing complete structural models of graphene. So far, deep insights into dislocations in graphene have been primarily from a theoretical perspective (*10–12*).

Experimental investigation of dislocations in graphene at the atomic level needs high-resolution imaging, with spatial resolution sufficient to unambiguously resolve individual carbon atoms. Low-voltage transmission electron microscopy (TEM) can resolve the lattice structure of carbon-based materials such as graphitic nanomaterials and graphene (*13–19*) with high contrast and minimal damage. Improvement in the information limit in high-resolution TEM (HRTEM) requires the reduction of both spherical and chromatic aberration, with the latter having a notable effect at low voltages. Spherical aberration correction in HRTEM, combined with low accelerating voltage operation to reduce knock-on damage [at less than 90 kV (*20*)], enables imaging of light-element atoms (including C, B, and N) in nanomaterials and molecules (*14*).

To image single–carbon atom dynamics in graphene using HRTEM, sufficient information transfer to unambiguously resolve the atomic positions is necessary. At low accelerating voltage, this cannot be achieved by spherical aberration correction alone and requires reducing chromatic aberration. Electron optical correction of chromatic aberration has been successfully reported (*21*, *22*). Alternatively, the use of a monochromator to reduce the energy spread in the incident electron beam provides a way of limiting chromatic effects (*23*). There have been several reports of HRTEM imaging of graphene both with (*24*) and without (*25*, *26*) monochromation at an accelerating voltage of 80 kV, but only relatively small differences in the resolution of images have been demonstrated. Indirect exit-wave reconstruction has also been used to characterize a fully resolved atomic structure for a monolayer/bilayer interface (*27*). However, this technique requires numerous images to generate the complex exit wave and is thus not suitable for the investigation of real-time single-atom dynamics, which are essential for monitoring structural transformations.

In this paper, we present low-voltage HRTEM imaging of dislocation dynamics in graphene, using both spherical aberration correction and monochromation of the electron beam using a double Wien filter (figs. S1 to S4). Graphene samples were prepared using chemical vapor deposition (CVD) on copper foils (*28*) and were transferred onto silicon nitride TEM grids with 2-μm holes (see the supplementary materials for details) (*29*).

Figure 1A shows a single HRTEM image of monolayer graphene containing a pair of edge dislocations aligned in opposite directions with (1,0) form, consisting of a pentagon-heptagon pair (*10*). Previous work has suggested the presence of a single dislocation in graphene (*19*) and a pair of dislocations in reduced graphene oxide (*30*), but the image resolution in those studies was not sufficient to resolve the individual atomic positions required to determine the exact structure. Figure 1B shows an atomic model, and Fig. 1C shows the multislice HRTEM image simulation for the dislocation pair observed in Fig. 1A.

There are five possible mechanisms that describe how these dislocation pairs could have formed: during the CVD growth, electron beam sputtering of carbon dimers along a zig-zag lattice direction, from surface adatom incorporation, from a mono vacancy, or from a Stone-Wales defect (figs. S5 to S7). Initial observation of the area of the sample in Fig. 1 showed that it was free from dislocations and monovacancies (fig. S8), which indicates that the dislocations were
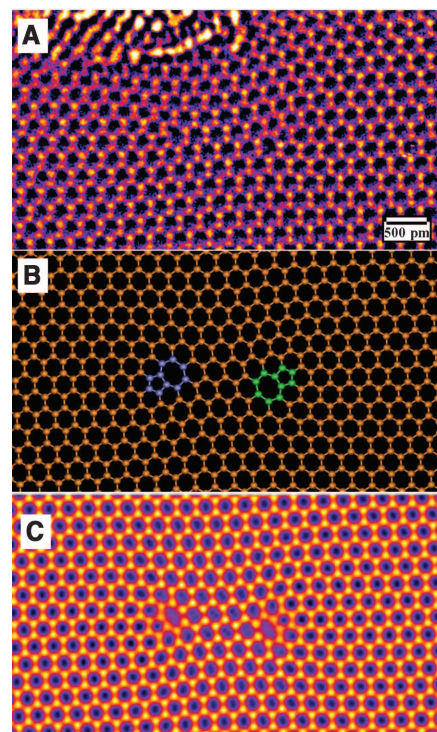
Fig. 1. Imaging edge dislocations. (**A**) HRTEM image showing two opposing (1,0) edge glide dislocations in graphene. (**B**) Structural model representing the dislocation pair (blue and green) in (A). (**C**) HRTEM image simulations using the atomic model in (B) as a supercell. False color is used for the images to aid visual inspection.

[1]Department of Materials, University of Oxford, Parks Road, Oxford OX1 3PH, UK. [2]JEOL, 3-1-2 Musashino, Akishima, Tokyo 196-8558, Japan.

*To whom correspondence should be addressed. E-mail: jamie.warner@materials.ox.ac.uk

formed after synthesis, probably through energy supplied by electron beam irradiation. The dislocation pairs we observed did not share a common glide plane, indicating that one dislocation had moved along the armchair direction at some stage. This process is known to stabilize dislocation dipoles and prevent their rapid annihilation (7).

Having two dislocations in graphene leads to strain fields that depend on their separation. We mapped the stain fields using the geometric phase analysis (GPA) method (31). Figure 2A shows a HRTEM image of a pair of dislocations in graphene, and Fig. 2B shows the corresponding GPA phase map obtained from Bragg spot b (fig. S9i). The phase map has two discontinuities of 2π, which is typical of dislocations (31). The strain tensor was made symmetric, leading to strain fields ε_{xx}, ε_{xy}, and ε_{yy}, and a rotation ω (in radians), shown in Fig. 2, C to F, respectively. The color scale mapping (Fig. 2C) has range −1 (black) to +1 (white). The strain ε_{xy} (Fig. 2D) corresponds to shear with values ranging from ~ 8 to 77% at distances of 0.1 to 0.02 nm from the dislocation core. The lattice rotation (Fig. 2F) has values ranging from ~15° to ~63° at distances of 0.1 to 0.02 nm from the dislocation core. The strain maps in Fig. 2 show that the strain fields from each dislocation core extend far enough to intersect. A similar analysis of regions of graphene containing closed loops of heptagons and pentagons did not produce such extended strain, and examination of pairs of dislocations with different separation lengths revealed the extent of the intersection (figs. S9 to S11). We compared the 2D profile of the strain fields to those predicted by the isotropic elastic, Peierls-Nabarro (PN), and Foreman (FM) dislocation theory models (fig. S12). The dislocations in graphene can be described by a PN model, but improvement is seen with the FM model, with fitting parameter of a = 1.5 (figs. S13 and S14).

During imaging, once the dislocation pair appeared (Fig. 3, A to D), it remained stable for 129 s under electron beam irradiation before a rapid transformation within 1 to 2 s to a new stable configuration (Fig. 3, B and E). This transformation corresponds to the minimum step single bond rotation along the zig-zag lattice direction, similar to dislocation creep. The dislocations remained stable in this configuration for a further 180 s and then rapidly transformed by the loss of two carbon atoms to move horizontally along the zig-zag lattice direction (Fig. 3, C and F), similar to dislocation climb. Tracking of the strain fields with dislocation movement showed that they remained focused around the dislocation cores and the central region between them (fig. S15).

We used density functional theory (DFT) in order to gain insights into the formation energy and bond lengths of the observed dislocation pair. The experimental studies have shown that a stable dislocation pair requires a mixture of glide (Stone-Wales bond rotation) and climb (removal
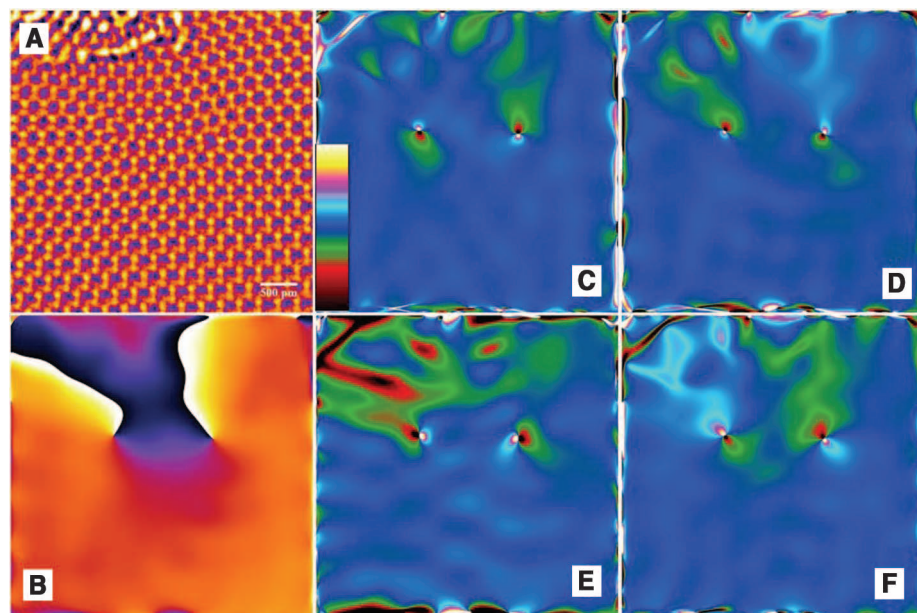

Fig. 2. Strain field mapping. (**A**) HRTEM image of a dislocation pair in graphene. GPA was applied to the HRTEM image in (A) to determine (**B**) the phase map, (**C**) ε_{xx}, (**D**) ε_{xy}, (**E**) ε_{yy}, and (**F**) rotation (in radians). The color scale for (C) to (F) is shown in (C), with a range of −0.5 (black) to +0.5 (white). For the phase map in (B), the color map is black (0) to white (2π).
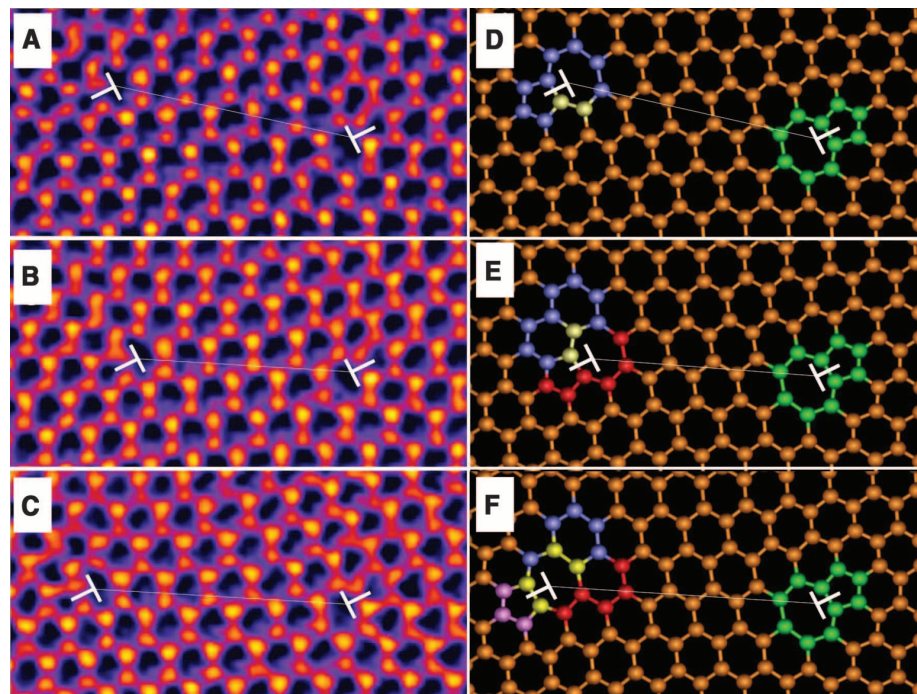

Fig. 3. Real-time dislocation dynamics. HRTEM images showing changes in the position of an edge glide dislocation with time under continuous electron beam irradiation. (**A**) Time = 0 s. (**B**) Time = 141 s. (**C**) Time = 321 s. (**D** to **F**) Atomic models illustrating the structures inferred from (A) to (C), respectively. The white T indicates the position of dislocation.

of two atoms) processes. These two mechanisms enable a pentagon-heptagon pair to migrate through a 2D lattice as a composite object. Our calculations of various stages of separated dislocation pairs in pristine graphene mediated by Stone-Wales bond rotations (Fig. 4, A to C) revealed

that for each subsequent step, the formation energy increase is at most 5.4 eV. The DFT formation energies of these structures for up to six bond rotations are shown in Fig. 4C as black dots. The formation energies incorporating corrections for long-range strain field interactions

Fig. 4. (**A** and **B**) Atomistic models obtained within DFT for one and four Stone-Wales bond rotations (steps 1 and 4). (**C**) Formation energy at each step (one dislocation is stationary and the other one is moving along the glide direction). The black dots represent the DFT data. The red dots represent the DFT data corrected for long-range strain-field interactions. (**D**) Total charge density of the structure shown in Fig. 3B. (**E**) C-C bond lengths in picometers for the structure in Fig. 4D extracted from the DFT calculations. (**F**) HRTEM image [Ice color look-up table (LUT)] of a dislocation pair with measurements of bond lengths in picometers. (**G**) HRTEM image (ice color LUT) of pristine graphene with measurement of bond lengths in picometers. The average C-C bond length was determined as 141 ± 10 pm.
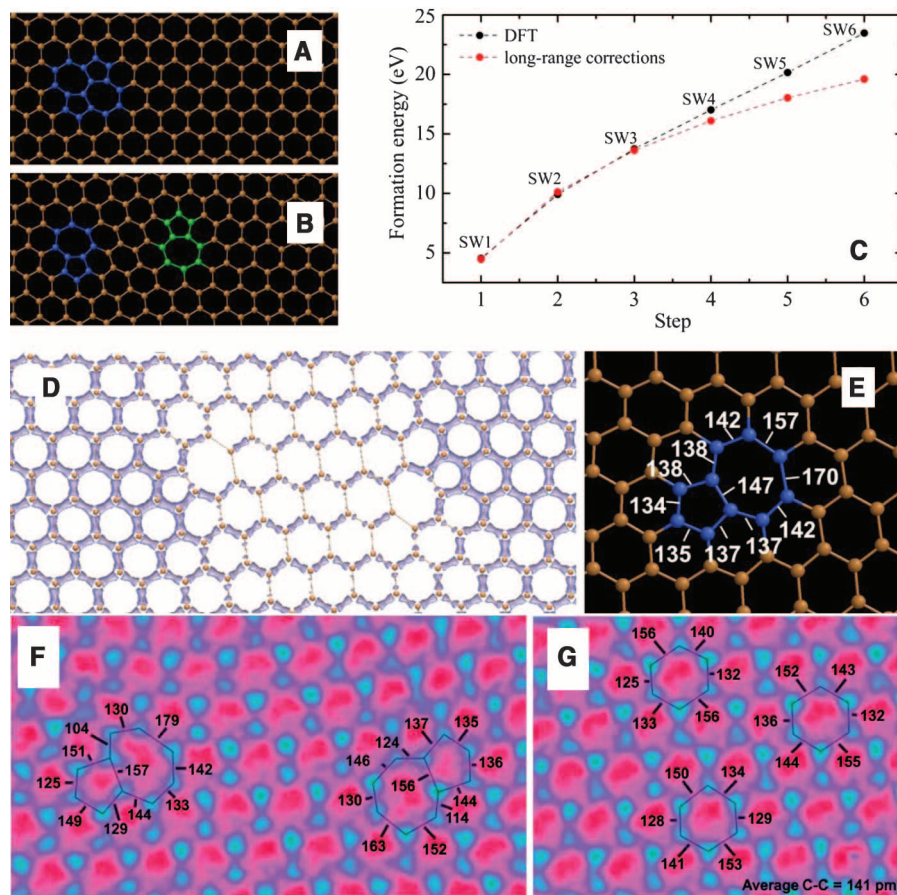
between periodic replicas of the dislocation pairs are shown by red dots in the same figure (fig. S16). The calculation details are provided in the supplementary materials. Another way of splitting two pentagon-heptagon dipoles in graphene consists of removing one carbon dimer at a time along the zig-zag direction. The formation energies involved in these processes are similar to those calculated here [see Jeong *et al.* (*12*)]. At each transition step (bond rotation or dimer removal), an energy activation barrier must be overcome. For a bond rotation (glide step), the energy barrier lies in the range of 5 to 10 eV, depending on the local atomic configuration of the sp^2-bonded carbon structure (*20, 32*). For each climb step, the energy barrier to remove a carbon dimer from the side of a pentagon is in the range of 9 to 12 eV (*33*). Overall, these energy barriers are comparable with the energy that is transferred by 80-keV electrons to carbon atoms, and therefore the processes described here are viable.

We calculated the formation energy of the dislocation pair in Fig. 1A to be 30.6 eV. Long-range strain-field corrections (Fig. 4C) reduce this to 26.7 to 28.5 eV. Our DFT formation energy is comparable with those reported for a dislocation obtained by removing a zig-zag carbon chain and for a haeckelite structure, when the number of missing carbon atoms is the same (*12*). The presence of the structural defects causes

elongation of the C-C bonds of the hexagons between the two dislocation dipoles (average bond length, 147 pm) and a substantial depletion of charge in this region (Fig. 4D). Overall, the bond length values vary from 134 to 170 pm for the pentagon-heptagon pair and from 136 pm to 141 pm in the graphene region with the lowest strain. The longest bond of the heptagon rings of 170 pm is similar to the 168 pm value reported in (*12*) for the dislocation structure with 10 vacancy units. All the bond lengths in our pentagon-heptagon dipole are shown in Fig. 4E.

Figure 4F shows an experimental HRTEM image with direct measurements of the bond lengths for a dislocation pair. The left dislocation has bond lengths from 104 to 179 pm, and the right from 114 to 163 pm. Bond lengths measured in regions of graphene where the elastic strain was minimal (Fig. 4G) were between 125 and 156 pm (hexagon 1), 132 and 155 pm (hexagon 2), and 128 and 153 pm (hexagon 3), yielding an average of 141 ± 10 pm, which agrees well with expected values. This corresponds to a maximum of 26% compression and 27% elongation of certain individual C-C bonds. The bonds with contraction or elongation are at the same position in each dislocation. The position of elongation matches that predicted by DFT, with some discrepancies likely to arise from possible warping and rippling of the graphene. Bond elongation cannot mistakenly arise because of a 2D projec-

tion of an out-of-plane distortion, such as rippling, and therefore is real.

We have shown that edge dislocations result in substantial deformation of the atomic structure of graphene, with bond compression or elongation of ±27%, plus shear strain and lattice rotations. If dislocation pairs are separated by less than 1.5 nm, the individual strain fields associated with each dislocation core intersect, and the presence of one dislocation affects the other. Energy from electron beam irradiation induced variation in the distance between the two dislocations in the pair, and tracking of the strain field showed that it remained localized around the core. Monochromation of the electron beam for HRTEM using a double Wien filter led to substantially improved image resolution that enabled the position of single carbon atoms to be accurately mapped.

References and Notes
1. C. Lee, X. Wei, J. W. Kysar, J. Hone, *Science* **321**, 385 (2008).
2. K. S. Novoselov *et al.*, *Science* **306**, 666 (2004).
3. A. Mesaros, D. Sadri, J. Zaanen, *Phys. Rev. B* **79**, 155111 (2009).
4. J.-H. Chen, L. Li, W. G. Cullen, E. D. Williams, M. S. Fuhrer, *Nat. Phys.* **7**, 535 (2011).
5. R. R. Nair *et al.*, *Nat. Phys.* **8**, 199 (2012).
6. N. Levy *et al.*, *Science* **329**, 544 (2010).
7. A. Carpio, L. L. Bonilla, *Phys. Rev. B* **78**, 085406 (2008).
8. S. Chen, D. C. Chrzan, *Phys. Rev. B* **84**, 214103 (2011).

9. R. Grantab, V. B. Shenoy, R. S. Ruoff, *Science* **330**, 946 (2010).
10. O. V. Yazyev, S. G. Louie, *Phys. Rev. B* **81**, 195420 (2010).
11. E. Cockayne *et al.*, *Phys. Rev. B* **83**, 195425 (2011).
12. B. W. Jeong, J. Ihm, G.-D. Lee, *Phys. Rev. B* **78**, 165403 (2008).
13. J. H. Warner, N. P. Young, A. I. Kirkland, G. A. D. Briggs, *Nat. Mater.* **10**, 958 (2011).
14. O. L. Krivanek *et al.*, *Nature* **464**, 571 (2010).
15. K. Suenaga, M. Koshino, *Nature* **468**, 1088 (2010).
16. J. Kotakoski, A. V. Krasheninnikov, U. Kaiser, J. C. Meyer, *Phys. Rev. Lett.* **106**, 105505 (2011).
17. J. C. Meyer *et al.*, *Nat. Mater.* **10**, 209 (2011).
18. P. Y. Huang *et al.*, *Nature* **469**, 389 (2011).
19. A. Hashimoto, K. Suenaga, A. Gloter, K. Urita, S. Iijima, *Nature* **430**, 870 (2004).
20. F. Banhart, J. Kotakoski, A. V. Krasheninnikov, *ACS Nano* **5**, 26 (2011).
21. B. Kabius *et al.*, *J. Electron Microsc. (Tokyo)* **58**, 147 (2009).
22. M. Haider, P. Hartel, H. Müller, S. Uhlemann, J. Zach, *Microsc. Microanal.* **16**, 393 (2010).
23. M. Mukai *et al.*, *Microsc. Microanal.* **11**, 2134 (2005).
24. J. C. Meyer *et al.*, *Nano Lett.* **8**, 3582 (2008).
25. J. H. Warner *et al.*, *Nat. Nanotechnol.* **4**, 500 (2009).
26. Z. Liu, K. Suenaga, P. J. F. Harris, S. Iijima, *Phys. Rev. Lett.* **102**, 015501 (2009).
27. J. R. Jinschek, E. Yucelen, H. A. Calderon, B. Freitag, *Carbon* **49**, 556 (2011).
28. X. Li *et al.*, *Science* **324**, 1312 (2009).
29. A. W. Robertson *et al.*, *ACS Nano* **5**, 6610 (2011).
30. C. Gómez-Navarro *et al.*, *Nano Lett.* **10**, 1144 (2010).
31. M. J. Hÿtch, E. Snoeck, R. Kilaas, *Ultramicroscopy* **74**, 131 (1998).
32. Y. Kim, J. Ihm, E. Yoon, G.-D. Lee, *Phys. Rev. B* **84**, 075445 (2011).
33. F. Ding, K. Jiao, Y. Lin, B. I. Yakobson, *Nano Lett.* **7**, 681 (2007).

A Reduced Organic Carbon Component in Martian Basalts

A. Steele,[1]* F. M. McCubbin,[1,2] M. Fries,[3] L. Kater,[4] N. Z. Boctor,[1] M. L. Fogel,[1] P. G. Conrad,[5] M. Glamoclija,[1] M. Spencer,[6] A. L. Morrow,[6] M. R. Hammond,[6] R. N. Zare,[6] E. P. Vicenzi,[7] S. Siljeström,[8,9] R. Bowden,[1] C. D. K. Herd,[10] B. O. Mysen,[1] S. B. Shirey,[11] H. E. F. Amundsen,[12] A. H. Treiman,[13] E. S. Bullock,[14] A. J. T. Jull[15]

The source and nature of carbon on Mars have been a subject of intense speculation. We report the results of confocal Raman imaging spectroscopy on 11 martian meteorites, spanning about 4.2 billion years of martian history. Ten of the meteorites contain abiotic macromolecular carbon (MMC) phases detected in association with small oxide grains included within high-temperature minerals. Polycyclic aromatic hydrocarbons were detected along with MMC phases in Dar al Gani 476. The association of organic carbon within magmatic minerals indicates that martian magmas favored precipitation of reduced carbon species during crystallization. The ubiquitous distribution of abiotic organic carbon in martian igneous rocks is important for understanding the martian carbon cycle and has implications for future missions to detect possible past martian life.

Organic carbon in macromolecular reduced form has been detected in several martian meteorites, but there is little agreement on its provenance on Mars. Hypotheses for its origin include terrestrial contamination (*1*, *2*), chondritic meteoritic input (*3*), thermal decomposition of carbonate minerals (*4–6*), direct precipitation from aqueous fluids (*4*), and the remains of ancient biota (*7*). Confirming the presence and understanding the source and formation of this reduced carbon has implications for the carbon budget of Mars, its putative carbon cycle, carbon availability for biotic chemistry, life detection, and how to detect organic compounds on future Mars missions.

Eleven martian meteorites, including samples of the recent Tissint meteorite fall, were studied with confocal Raman imaging spectroscopy (CRIS). Macromolecular carbon (MMC) was identified in 10 of these meteorites associated with small (2 to 20 µm) metal oxide grains (hereafter referred to as spinel or oxide) that are ubiquitous as inclusions within olivine and/or pyroxene grains (Fig. 1 and fig. S1) (*8*). All of the MMC that we report here was located at least several microns below the top surface of the thin sections we analyzed (Fig. 1). The association of MMC with spinel is observed in recent falls (Tissint and Zagami), as well as older finds (DaG 476 and SAU 019) (table S1), making it unlikely to be terrestrial contamination (*9*).

MMC is characterized by the diagnostic disordered "D" Raman peak at ~1350 and the graphitic ordered peak at ~1590 cm^{-1} (Fig. 2, A and B) (*10*, *11*). MMC was initially detected within olivine-hosted melt inclusions in DaG 476 in association with oxide and pyroxene (table S1). DaG 476 is an olivine-phyric shergottite with olivine comprising 15 to 17% of the mode (fig. S1, A to E) (*12*). The oxides are fine-grained spinel-group minerals that appear to be magnetite or chromite based on the Raman peak positions. They are distributed throughout the olivine with enough grains below the surface to allow study of associated MMC that is completely encased within a silicate host (Fig. 1, A to F). With a combination of transmitted and reflected light, we determined the distance from the oxides to the surface and confirmed their isolation from any visible cracks (Fig. 1G). Figure 1G shows a three-dimensional (3D) CRIS depth profile of MMC occurring with spinel at a distance of 5 to 10 µm into the surface of DaG 476. Scanning electron microscopic (SEM) investigations of DaG 476 and SAU 130 showed oxides containing a carbon film that is texturally and chemically consistent with the MMC observed by CRIS (fig. S3) and is neither carbonate nor terrestrial microbial contamination (*12–14*).

Transmitted-light microscopy images and CRIS peak maps of a number of oxide grains hosted by pyroxenes in ALH 84001 and olivines from northwest Africa (NWA) 1110 demonstrate the co-occurrence of MMC phases with oxides in other meteorites analyzed (Fig. 1, H and I). In the

[1]Geophysical Laboratory, Carnegie Institution of Washington, 5251 Broad Branch Road, NW, Washington, DC 20015, USA. [2]Institute of Meteoritics, Department of Earth and Planetary Sciences, University of New Mexico, Albuquerque, NM 87131, USA. [3]Planetary Science Institute, 1700 East Fort Lowell, Suite 106, Tucson, AZ 85719, USA. [4]Witec GmbH, Lise-Meitner-Strasse 6, D-89081, Ulm, Germany. [5]NASA Goddard Space Flight Centre, 8800 Greenbelt Road, Greenbelt, MD 20771, USA. [6]Department of Chemistry, Stanford University, Stanford, CA 94305, USA. [7]Museum Conservation Institute, Smithsonian Institution, 4210 Silver Hill Road, Suitland, MD 20746, USA. [8]Department of Geological Sciences, Stockholm University, 10691 Stockholm, Sweden. [9]Department of Chemistry and Materials, SP Technical Research Institute of Sweden, 501 15 Borås, Sweden. [10]Department of Earth and Atmospheric Sciences, University of Alberta, Edmonton, AB T6G 2E3, Canada. [11]Department of Terrestrial Magnetism, Carnegie Institution of Washington, 5241 Broad Branch Road, NW, Washington, DC 20015, USA. [12]Earth and Planetary Exploration Services, Jacob Aals Gate 44b, 0364 Oslo, Norway. [13]Lunar and Planetary Institute, 3600 Bay Area Boulevard, Houston, TX 77058, USA. [14]Department of Mineral Sciences, Smithsonian Institution, Washington, DC 20013–7012, USA. [15]University of Arizona, 1118 East Fourth Street, Tucson, AZ 85721, USA.

*To whom correspondence should be addressed. E-mail: asteele@ciw.edu